$Ba_2Co_9O_{14}$: New Inorganic Building Blocks with Magnetic Ordering through Super-Super Exchanges Only

Ghislaine Ehora,[†] Sylvie Daviero-Minaud,[†] Marie Colmont,[†] Gilles André,[‡] and Olivier Mentré*,[†]

Unité de Catalyse et de Chimie du Solide, Equipe de Chimie du Solide UMR-CNRS-8181, USTL/ENSCL, bât. C7, 59652 Villeneuve d'Ascq cedex, France, and Laboratoire Léon Brillouin, UMR CNRS 12, CEA-Saclay, bât. 563-91191 Gif-sur-Yvette Cedex, France

Received December 7, 2006. Revised Manuscript Received February 15, 2007

$Ba_2Co^{2+}{}_3Co^{3+}{}_6O_{14}$ has been prepared by conventional solid-state reaction between BaO_2 and CoO. Its crystal structure has been refined from single-crystal X-ray diffraction data and powder neutron diffraction, $a = 5.6963(8)$ Å, $c = 28.924(6)$ Å, space group $R\bar{3}m$, $Z = 3$, R1 = 4.44%, wR2 = 10.96%. It shows evidence of new building blocks called T′ (ch′h′c stacking sequence of cubic O_4 and hexagonal BaO_3 layers) by analogy with the related T-blocks (hh′h′h) of the barium hexaferrites. T′ consists of $Co^{II,III}O_2$ brucite-like layers pillared by $Co^{II}O_4$ tetrahedra and $Co^{III}{}_3O_{12}$ octahedral trimers. Below $T_N = 39$ K, tetrahedral and octahedral high spin Co^{II} ($S = 3/2$) diluted in the framework mainly containing low spin Co^{III} ($S = 0$) interact through $Co^{II}-O-O-Co^{II}$ through super-super exchanges (SSE) only. The analysis of the competition between the multiple SSE paths has been performed through geometrical considerations. The magnetic moments are lying antiferromagnetically in the *a,b* plane in good agreement with the magnetic group theory presented in our work. Their values of 1.70(4) μB and 2.83(3) μB for the octahedral and tetrahedral Co^{II}, respectively, are explained by the high degree of covalency and magnetic transfer toward the surrounding anions involved in the SSEs. At high temperature, the creation of oxygen vacancies is observed and strongly intervenes in the hopping conductivity as shown from the abrupt change in the matching Arrhenius law. This particular feature demonstrates potential mixed conductivity processes in the medium-temperature range. At 1000 °C, it reversibly decomposes into CoO and $BaCoO_{3-\delta}$. Finally, the medium crystallinity of the title compound is explained by the presence of defects and intergrowths with other hexagonal perovskites of the Ba−Co−O system.

Introduction

The possibility to build up new mineral frameworks from the stacking of cubic (c) and/or hexagonal (h) anionic layers appears unlimited, as pictured by the unlimited number of hexagonal perovskite polymorphs. Then the compounds could have dimensional characteristics that range between the ideal three-dimensional (3D) 3C perovskite (c layers only) and the one-dimensional 2H-$BaNiO_3$ type (h layers only).[1] In addition, the possible existence of oxygen vacancies also plays a major role on the chemistry of these solids. As a matter of fact, the metal valence is generally related to a given coordination, then ruling out the stacking arrangements. Examples such as the $BaFeO_{3-\delta}$ case picture well this structural versatility because the distribution of the oxygen vacancies is related to the possible pyramidal or tetrahedral coordination of Fe^{III}; for example, starting from the 2H-$BaFeO_3$, two polytypes are reported: the 12H type for $0.07 \leq \delta \leq 0.13$[2] and the 6H type for $0.20 \leq \delta \leq 0.35$.[3,4] Differently, the $BaMnO_{3-\delta}$ system is accommodated by the strong preference of deficient $BaO_{2.5}$ layers for cubic stacking.[5,6] It leads to series 15-R $BaMnO_{2.90}$, 8-H $BaMnO_{2.875}$, 6H-$BaMnO_{2.833}$, 10H-$BaMnO_{2.80}$, 4-H $BaMnO_{2.75}$, 21-R $BaMnO_{2.92-2.88}$, and so forth.[7] Closer to the title compound, from the 2H-$BaCoO_3$ system two oxygen deficient polytypes have been reported, the 5H form for $\delta \sim 0.26$[8,9] and the 12H form for $\delta \sim 0.4$.[10] These two structural types show the same structural units as $Ba_5Co_5ClO_{13}$[11] and the recently evidenced $Ba_6Co_6ClO_{16-\delta}$,[12] that is, trimers and tetramers of face sharing Co^{III} octahedra sharing their corners with Co^{IV} tetrahedra. Note that the title compound displays similar trimers. To be exhaustive, one should keep in mind

* Corresponding author. E-mail: mentre@ensc-lille.fr.
† UMR-CNRS-8181.
‡ UMR CNRS 12.

(1) Lander, J. J. *Acta Crystallogr.* **1951**, *4*, 148.
(2) Parras, M.; vallet-Regì, M.; Gonzàlez-Calbet, J. M.; Grenier, J. C.; Hagenmuller, P. Rodriguez-Carvajal, J. *Eur. J. Solid State Inorg. Chem.* **1989**, *26*, 299.
(3) Parras, M.; Vallet-Regì, M.; Gonzàlez-Calbet, J. M.; Grenier, J. C. *J. Solid State Chem.* **1989**, *83*, 121.
(4) Jacobson, A. J. *Acta Crystallogr. Sect., B* **1976**, *32*, 1087.
(5) Parras, M.; Alonso, J.; Gonzàlez-Calbet, J. M.; vallet-Regì, M. *J. Solid State Chem.* **1994**, *111*, 202.
(6) Parras, M.; Gonzàlez-Calbet, J. M.; Alonso, J.; Vallet-Regì, M. *J. Solid State Chem.* **1995**, *117*, 21.
(7) Quarez, E.; Roussel, P.; Pérez, O.; Leligny, H.; Bendraoua, A.; Mentré, O. *Solid State Sci.* **2004**, *6*, 931.
(8) Parras, M.; Varela, A.; Seehofer, H.; Gonzalez-Calbet, J. M. *J. Solid State Chem.* **1995**, *120*, 327.
(9) Boulahya, K.; Parras, M.; Gonzalez-Calbet, J. M.; Amador, U.; Martinez, J. L.; Tissen, V.; Fernandez-Diaz, M. T. *Phys. Rev. B* **2005**, *71*, 144402.
(10) Jacobson, A. J.; Hutchison, J. L. *J. Solid State Chem.* **1980**, *35*, 334.
(11) Yamamura, K.; Young, D. P.; Siegrist, T.; Besnard, C.; Svensson, C.; Liu, Y.; Cava, R. J. *J. Solid State Chem.* **2001**, *158*, 175.
(12) Tancret, N.; Roussel, P.; Abraham, F. *J. Solid State Chem.* **2005**, *178*, 3066.

10.1021/cm062897q CCC: $37.00
Published on Web 03/27/2007

the discovery from the Ba−$Co^{III/IV}$−O phase diagram of a number of incommensurate bidimensional compounds formed from the intergrowth between units with the 2H-$BaNiO_3$[1] and Sr_4PtO_6 types.[13] It gives rise to columns formed from the face sharing octahedra and prisms stabilized by the mixed Co^{III}/Co^{IV} valence, for example, $Ba_8Co^{+3.71}{}_7O_{21}$,[14] $Ba_{1.1064}Co^{+3.78}O_3$,[15] $Ba_{12}Co^{+3.82}{}_{11}O_{33}$,[16] $Ba_9Co^{+3.75}{}_8O_{24}$,[17] and so forth. General features about this wide $A_{n+2}Co_{2n+1}O_3$ family are given in refs 18 and 19. In the today's context, the interest for cobaltites has been renewed by the recent discovery of superconductivity and attractive thermoelectric properties in Na_xCoO_2 and their hydrated derivatives.[20] In addition, the search for oxides as potential low-temperature electrodes for solid oxide fuel cells (SOFCs) remains a key activity in today's solid-state chemistry. Hence, considering the prospect for new cobalt-based oxides has become a challenge for solid-state chemists. Indeed, we have isolated the new mixed $Co^{II,III}$ oxide $Ba_2Co_9O_{14}$. As a result of the similarities between the solid-state chemistry of cobalt and iron, for example, comparable ionic radii, competition between high spin and low spin configurations and duality between octahedral/tetrahedral coordination for Co^{II} similar to the tetrahedral/pyramidal/octahedral competition in mixed $Fe^{II/III}$ oxides (see the Fe/Co solid solutions in ferrites $Ba_3Co_{2-x}Fe_{24+x}O_{41}$,[21] $BaCo_{2-x}Fe_{16+x}O_{27}$,[22] etc.), the structural relationship with the barium hexaferrites has been pointed out. Thus, it has been shown that $Ba_2Co_9O_{14}$ is the first example of T′-block-like structure, an elemental motif related to the well-known T building blocks of ferrites never isolated until today. It shows the setting of an antiferromagnetic (AF) magnetic ordering below $T_N = 39$ K, by Co^{II}−O−O−Co^{II} super-super exchanges (SSEs), intensively discussed here. Intra- and inter-block electronic interactions have been analyzed through the pertinent geometrical parameters. Thermal analyses show the creation of oxygen vacancies that strongly influence the bulk conductivity, suggesting potential electrochemical applications.

Experimental Section

Synthesis. The single crystals have been prepared by slow cooling (3 °C/h) from 900 °C to room temperature of a mixture of BaO_2 and CoO in the flux-like BaF_2−NaF mixture in the 1:2:2:1 ratio sealed in a gold tube. After the thermal treatment, black single crystals can be isolated from the inhomogeneous products. The $Ba_2Co_9O_{14}$ powder preparation is achieved from a stoichiometric mixture of BaO_2 and CoO powders heated (2.5 °C/mn) at 900 °C for 72 h with intermediate grindings and finally slowly cooled (1.5 °C/mn) down to room temperature. It is noticeable that, upon extra heating stages, the crystallinity of the compound is getting worse while weak peaks of a second phase appear on the X-ray diffraction (XRD) patterns.

Table 1. Crystal and Refinement Data

Crystal Data ($T = 293$ K)	
symmetry	rhombohedral
space group	$R\bar{3}m$ (No. 166)
unit cell (Å)	$a = 5.6963(8)$
	$c = 28.924(6)$
	$V = 812.79(19)$ Å^3
Z	3
Data Collection	
equipment	Bruker Smart -1K
λ (Mo Kα (graphite monochromator); Å)	0.7107
density calcd (g/cm^3)	6.307
color	black
scan mode	ω scans
Θ(min−max) (deg)	2.11−28.08
μ (mm^{-1}; for λKα = 0.7107 Å)	20.612
T_{min}/T_{max}	0.373
R(int) (%)	7.36
recording reciprocal space	$-7 \le h, k \le 7, -36 \le l \le 36$
number of measured reflections	1653
number of independent reflections ($I > 2\sigma(I)$), total	251/222
crystal dimensions (mm)	0.3 × 0.3 × 0.4
Refinement	
number of refined parameters	34
refinement method, program	L.S. on I, SHELXL
R1(F) [$I > 2\sigma I$]/R1(F) [all data, %]	4.44/5.09
wR^2(F^2) [$I > 2\sigma I$]/wR2(F^2) [all data, %], $w = 1/(\sigma^2(F_o^2) + (0.0682P)^2)$ with $P = (\max(F_o^2, 0) + 2F_c^2)/3$	10.96/11.20
GOF	1.073
max/min residual electronic density (e$^-$/Å^3)	3.09/−2.49
refined extinction coefficient	0.0013(4)

XRD and Neutron Diffraction (ND). The single-crystal XRD data collection was performed using a Bruker SMART CCD-1K diffractometer, Mo Kα radiation. The experimental details as well as the parameters of the refinement are listed in the Table 1. The intensities have been extracted using SAINT[23] and corrected from absorption effects by a redundancy algorithm using the program SADABS.[24] Powder XRD profiles were recorded with a Bruker D8 diffractometer equipped with a HTK 1200 oven-camera with environmental heater ($\Delta T = 25$ °C), Cu Kα radiation. We benefited from two sets of ND measurement: (i) high-resolution diffraction pattern, D2B diffractometer ($\lambda = 1.594$ Å) at the Institut Laue-Langevin (ILL), and (ii) 45 to 1.5 K temperature-dependent patterns : G41 ($\lambda = 2.426$ Å) at the Laboratoire Léon-brillouin (LLB). For the synthesis of a large amount of sample (typically 5−8 g), weak impurity peaks appear even after optimization of the number of grinding/heating stages. Few 2θ regions have been excluded in the data treatment. XRD and ND data were analyzed using the Rietveld method using the FULLPROF 2000 program.[25]

Thermal Analyses and Magnetic and Electric Measurements. Both thermogravimetric analysis (TGA) and differential thermal

(13) Randall, J. J.; Katz, L. *Acta Crystallogr*. **1959**, *12*, 519.
(14) Boulahya, K.; Parras. M.; Gonzalez-Calbet, J. M.; Vegas, A. *J. Solid State Chem*. **2000**, *151*, 77.
(15) El Abed, A.; Elqebbaj, S. E.; Zakhour, M.; Champeaux, M.; Perez-Mato, J. M.; Darriet. *J. Solid State Chem*. **2001**, *161*, 300.
(16) Darriet, J.; Elcoro, L.; El Abed, A.; Gaudin, E.; Perez-Mato, J. M. *Chem. Mater*. **2002**, *14*, 3349.
(17) Boulahya, K.; Parras, M.; Gonzalez-Calbet, J. M. *J. Solid State Chem*. **1999**, *142*, 419.
(18) Boulahya, K.; Parras, M.; Gonzalez-Calbet, J. M. *J. Solid State Chem*. **1999**, *145*, 116.
(19) Boulahya, K.; Parras, M.; Gonzalez-Calbet, J. M. *Chem. Mater*. **2000**, *12*, 25.
(20) Terasaki, I.; Sasago, Y.; Uchinokura, K. *Phys. Rev. B* **1997**, *56*, R12685.
(21) Tachibana, T.; Nakagawa, T.; Takada, Y.; Yamamoto, T. A.; Shimada, T.; Kawano, S. *J. Magn. Magn. Mater*. **2003**, *262*, 248.
(22) Collomb, A.; Wolfers, P.; Obradors, X. *J. Magn. Magn. Mater*. **1986**, *62*, 57.
(23) *SAINT: Area-Detector Integration Software*; Siemens Industrial Automation, Inc.: Madison, WI, 1995.
(24) *SADABS: Area-Detector Absorption Correction*; Siemens Industrial Automation, Inc.: Madison, WI, 1996.
(25) Rodriguez-Carvajal, J. *Physica B* **1993**, *192*, 55 (program Fullprof available from http://www-llb.cea.fr/fullweb/fp2k/fp2k.htm).

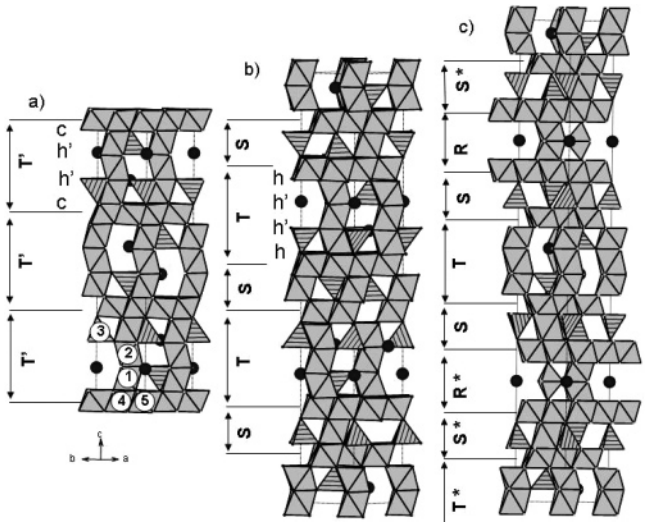

Figure 1. View of the T′-blocks in $Ba_2Co_9O_{14}$ (a) and the T-blocks in the Ba hexaferrite Y-type (b) and Z-type (c).

analysis (DTA) have been performed on a combined TG-DTA 92-1600 SETARAM analyzer through a heating/cooling cycle, 5 °C/min. The susceptibility ($H = 1$ T) and magnetization ($T = 4$ K, $H = 0-5$ T) have been measured by the direct current extraction method using an OXFORD Maglab EXA 9T system.

The electric transport has been measured from 4 to 923 K using a linear four equidistant platinum probes cell, on a sintered cylinder, $T_{sintering} = 900$ °C. Special details are given in the corresponding section. The resistivity was estimated from the resistance (R) as $\rho = (2\pi s/F_{(d/s)})R$ where s is the electrode spacing (=0.34 cm) and d is the cylinder diameter (=0.5 cm). In our experimental conditions, the geometric corrective $F_{(d/s)}$ term[26] is evaluated to be 0.075. For each temperature the voltage measurement was performed at $i = \pm i_0, \pm 2i_0$, and $\pm 10i_0$; $i_0 = 1$ mA showing a correct $i = f(u)$ linearity. At lower temperature the i value is 5 μA.

Electron Microscopy. The transmission electron microscopy (TEM) investigation was carried out with a JEOL JEM-3010 microscope operating at 300 kV ($C_s = 0.6$ mm, resolution 1.7 Å). Images were recorded with a CCD camera (model Keen View, SIS analysis, 1024 × 1024 pixels, pixel size 23.5 × 23.5 m). The powder sample was crushed for 1/2 h in an agate mortar to prevent effects from preferred orientation and crystal morphology, dispersed in ethanol by an ultrasonic method, and deposited on a holey carbon microgrid.

Results and Discussion

Crystal Structure. It was solved and refined using the SHELXTL suite.[27] The crystal structure is compatible with the centric space group $R\bar{3}m$ and subgroups $R32$ and $R\bar{3}$. The latest is rapidly eliminated, involving a split of some $R\bar{3}m$ independent positions. The latter has been selected, leading to better R values with the smallest number of refined parameters, Table 1. However, one should note the misleading acentric model ($R32$: R1 = 4.51%, wR2 = 5.18%; 41 parameters; same number of atoms, 9 atoms) that could be effective at low temperature through a symmetry lowering but undistinguishable considering the low resolution of ND experiments. However, our magnetic analysis by the group theory unambiguously assigns the $R\bar{3}m$ space group below T_N; see below. Figure 1a shows the 3D edifice projected along [110] with the label scheme for cobalt and evidence of the new T′ units.

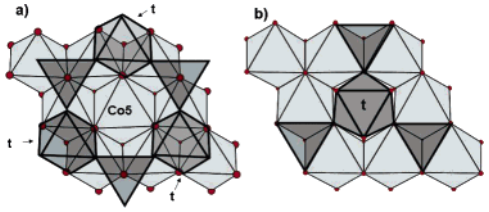

Figure 2. Projection along [001] of T′- (a) and T- (b) blocks where t shows the trimeric units.

Oxygen Vacancies. The Co redox dosage is described in Supporting Information. It yields an average value of +2.64 in good agreement with the expected +2.66 mean valence using the $Ba_2Co_9O_{14}$ formula at room temperature. Additionally, the crystal structure at room temperature was refined from high-resolution ND data, leading to atomic parameters nearly unchanged from our single-crystal results. The refinement of occupancies for the O1 and O3 lead to fully occupied positions. O2 is more questionable because it gives rise to occupancy ~ 90%. However, its constraining to a fully occupied position does not sensibly modify the refinement (less than 0.5% for R_{Bragg}) and yields the correct thermal parameter $B_{O2} \sim 0.30$ Å^{-1} ($R_{Bragg} = 5.30\%$, $R_F = 3.28\%$, $\chi^2 = 0.230$, $R_p = 15\%$, and $R_{wp} = 14.2\%$; see Supporting Information). In addition, O2 being part of the Co3 tetrahedral coordination, its partial occupancy is unlikely.

Description of the Structure. A number of hexaferrites have been reported in the literature and classified into several main classes according to their structure: M-type $Ba(Fe,M)_{12}O_{19}$, W-type $Ba(Fe,M)_{18}O_{27}$, X-type $Ba_2(Fe,M)_{30}O_{46}$, Y-type $Ba_2(Fe,M)_{14}O_{22}$, Z-type $Ba_3(M,Fe)_{26}O_{41}$, and so forth,[28] where M is a divalent transition metal including Co^{2+}. Their crystal structures are diversified and complex because they are built up from the packing along the hexagonal axis of different blocks, namely, R, S, T, superimposed differently. The Y-type[29] and the Z-type[20] are juxtaposed to $Ba_2Co_9O_{14}$ in Figure 1b,c. The former hexaferrite has a $(ST)_3$ packing sequence while the latter corresponds to the (STSRS*T*S*R*) sequence (where the * symbol denotes same blocks turned 180° around the c-axis). Therefore, the so-called T′ units in $Ba_2Co_9O_{14}$ and the T-blocks exhibit obvious but misleading similarities. They both contain slabs of edge sharing octahedra parallel to the hexagonal plane, linked together by pillars formed of trimers of face-sharing octahedra. The trimeric units are interconnected by corner sharing tetrahedra. However, the projection along [001] reveals important differences between them, Figure 2. It appears that because of their different closed-packing (ch′h′c, where h and c denote hexagonal and cubic O_4 layers while h′ stand for hexagonal BaO_3 layers) for T′ and (hh′h′h) for T, the former contains CdI_2 layers forming Brucite-like slabs while T-blocks display a Kagomé lattice. In the T′ units the trimeric pillar grows from three neighboring octahedra of

(26) Laplume, J. *Onde Electr.* **1955**, *335*, 113.
(27) Sheldrick, G. M. *SHELXTL*, suite version 5. 1; Bruker AXS: Madison, WI, 1998.
(28) Smith, J.; Wijn, H. B. J. *Ferrites*; Cleaver-Hume Press: London, 1959.
(29) Collomb, A.; Hadj Farhat, M. A.; Jourdel, J. C. *Mater. Res. Bull.* **1989**, *24*, 453.

Table 2. Interatomic Distances (Å) and Calculated Bond Valences (Σs_{ij}) of Cobalt Atoms in $Ba_2Co_9O_{14}$

Co1−O1 (×3)	1.923(6)	Co1−Co2	2.507(2)
Co1−O3 (×3)	1.947(6)	Co1−Co4 (×3)	2.838(1)
$\Sigma s_{ij} = 3.18$		Co1−Ba1 (×2)	3.4603(9)
Co2−O1 (×6)	1.945(6)	Co2−Co1 (×2)	2.507(2)
$\Sigma s_{ij} = 3.09$		Co2−Ba1 (×4)	3.5868(6)
Co3−O2	1.92(1)	Co3−Ba1 (×3)	3.3273(6)
Co3−O1 (×3)	1.934(7)	Co3−Ba1	3.368(2)
$\Sigma s_{ij} = 2.10$			
Co4−O3 (×4)	1.920(4)	Co4−Co5 (×2)	2.8482(4)
Co4−O2 (×2)	1.904(5)	Co4−Co1 (×2)	2.838(1)
$\Sigma s_{ij} = 3.36$		Co4−Co4 (×2)	2.8482(4)
Co5−O3 (×6)	2.082(6)	Co5−Co4 (×6)	2.8481 (4)
$\Sigma s_{ij} = 2.09$			
		Ba1−O1 (×3)	3.256(6)
		Ba1−O1 (×6)	2.8578(7)
		Ba1−O3 (×3)	2.907(6)

the slabs, while for T, it is at the top of the Kagomé window by sharing corners with six distinct octahedra. In both cases, the bases of the trimeric pillars are surrounded by three tetrahedra. To summarize, the crystal structure for $Ba_2Co_9O_{14}$ has a $(ch'h'c)_3$ layers sequence. It can be viewed as a T'_3 type crystal structure where the designation T′ is given by analogy with the T-blocks of Ba−hexaferrites.

The pertinent bond distances are reported in Table 2. The bond valence sums (BVS) have been calculated from Bresse and O'Keeffe data.[30] The octahedral Co1, Co2, and Co4 have mean Co−O distances that lie in the range from 1.90 to 1.95 Å, significantly shorter than Co5−O =2.08 Å in accordance with a Co^{III}/Co^{II} charge ordering. In addition, divalent states for both the octahedral Co5 and the tetrahedral Co3 likely leads to the neutral $Ba_2Co^{2+}{}_3Co^{3+}{}_6O_{14}$ formula. It is reinforced by the Co3−O and Co5−O distances similar to those observed in $Co_3(PO_4)_2$[31] also containing octahedral and tetrahedral divalent cobalt. The BVS calculation for Co4 is +3.4 and indicates a slightly over-bonded character. Actually, this effect is mainly due to the compact surrounding of the $Co4O_6$ units sharing four edges with other $Co4O_6$ octahedra, two edges with voluminous $Co5O_6$ octahedra, one edge with a trimeric pillar, and one corner with a $Co3O_4$ tetrahedron. The Co1−Co2 distance along the trimers is 2.507(2) Å, nearly similar to those found along Co^{III} octahedral tetramers in $Ba_6Co_6ClO_{16-\delta}$ (=2.48 Å)[12,32] and those found in the 5H-$BaCoO_{2.8}$ trimers (=2.47 Å).[8,9] In the latter, no Co^{III}/Co^{IV} segregation over octahedral (three per unit cell) and tetrahedral sites (two per unit cell) has been assumed by authors, but one should note that the slight barium-deficient character reported for the 12H-$Ba_{0.9}CoO_{2.6}$[33] (octa/tetra ratio = 1/2) matches rather well a possible $Co^{III}{}_{octa}/Co^{IV}{}_{tetra}$ charge ordering. As a matter of fact, for mixed valent Co^{III}/Co^{IV} linear oligomers found in the one-dimensional $A_{n+2}Co_{2n+1}O_3$ series[14,16,18] the Co−Co separation is shorter (~2.4 Å) in good agreement with Co^{IV} smaller ionic radii.

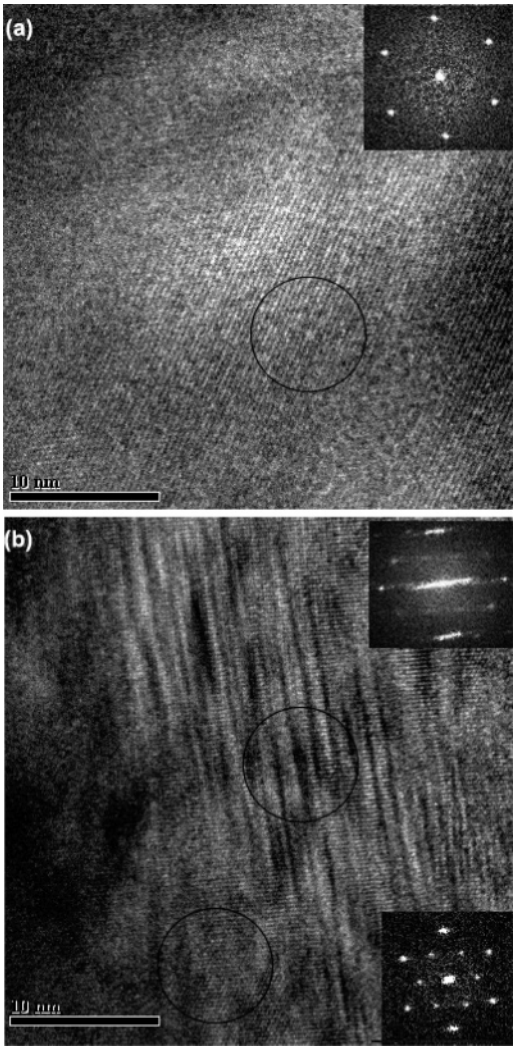

Figure 3. TEM image of $Ba_2Co_9O_{14}$ showing (a) predominantly large homogeneous domains (R Bravais lattice) and (b) intergrowth-like defects. The region bordering the defect is primitive.

Intergrowth. A preliminary study by electron diffraction (ED) corroborates the choice of the space group $R\bar{3}m$. The microcrystals related to it show large R-hexagonal lattices as calculated by FFT (fast fourier Transform) Figure 3a. However, for some crystals, important defected zones appear. They correspond to intergrowth in the *a*,*b* planes leading to diffuse streaks on the calculated ED patterns. Sometimes, single domains bordering the defects reveal a primitive superlattice, in good agreement with local structural and compositional changes. Particular points should be kept in mind for an overview of this result. (i) Let us recall that the crystallinity and purity of $Ba_2Co_9O_{14}$ is very sensitive to the preparation route, notably to the number of grinding/heating cycles. (ii) Most of the possible competing phases including ferrite-like structural types are built up from anionic layers generally leading to a comparable and hexagonal basis, $a \sim 5.5$ Å, likely for the intergrowth with $Ba_2Co_9O_{14}$.

Thermal Behavior. The TGA and DTA plots and the lattice parameters versus the temperature on heating are shown in Figure 4a,b. Between 300 °C and 800 °C the in-plane *a* parameter shows a weak shift from the linearity while *c* is characterized by a broad concave upward anomaly, related to the rounded drift of the TGA line. In that domain,

(30) Bresse, N. E.; O'Keeffe, M. *Acta. Crystallogr., Sect. B* **1991**, *47*, 192.
(31) Forsyth, J. B.; Wilkinson, C.; Paster, S.; Wanklyn, B. M. *J. Phys. C: Solid State Phys.* **1988**, *21*, 2005.
(32) Kauffmann, M.; Mentré, O.; Legris, A.; Tancret, N.; Abraham, F.; Roussel, P. *Chem. Phys. Lett.*, in press. Corrected proof available online October 2006.
(33) Maignan, A.; Hébert, S.; Pelloquin, D.; V. Pralong, V. *J. Solid State Chem.* **2006**, *179*, 1852.

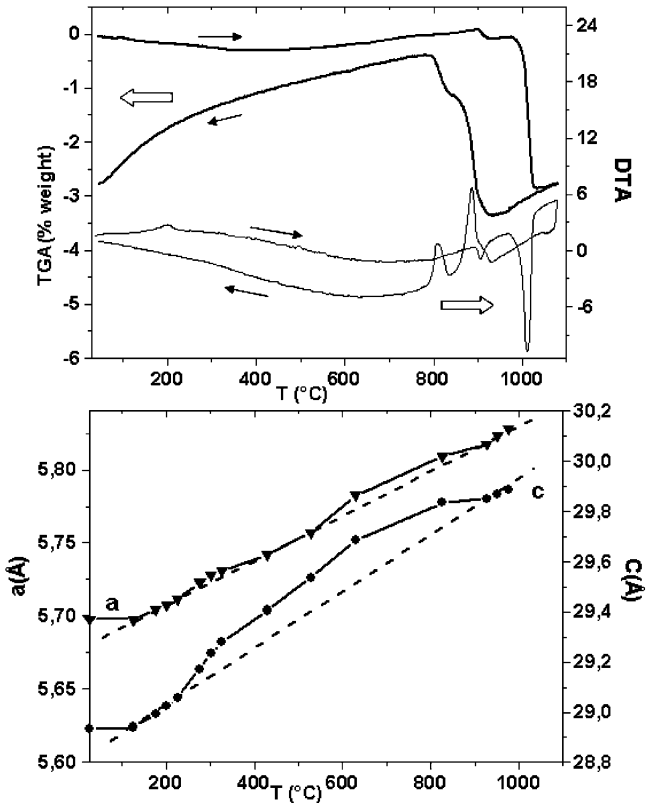

Figure 4. (a) TGA and DTA curves and (b) the lattice lattice paramaters versus *T*.

$Ba_2Co_9O_{14}$ could partially get reduced and reoxidizes under air with a maximal oxygen loss of 0.2 oxygen atoms per formula unit. This is in connection with the resistivity change shown below, in agreement with a real intrinsic modification of the material. A stationary regime is reached at 800 °C followed by the abrupt loss of ∼ 0.1 oxygen atoms per formula unit at ∼900 °C accompanied by a weak DTA peak. It is worth mentioning that between 900 °C and 1000 °C, the original unit cell is conserved with a linear dilatation versus *T*. The estimated coefficient of dilatation is 8×10^{-5} °C^{-1}. At 1030 °C, a sharp DTA peak is attributed to the decomposition of $Ba_2Co_9O_{14}$ into CoO and the cubic $BaCoO_{\sim 2}$. This phenomenon is accompanied by the loss of ∼1.6 oxygen atoms per formula unit. Surprisingly all the phenomena pointed out here are reversible across a large thermal hysteresis effect (ΔT heating−cooling ∼ 100 °C) yielding the alternative possibility to prepare $Ba_2Co_9O_{14}$ from the mixture of these two oxides.

Magnetic and Electric Properties. The Figure 5 presents χ^{-1} versus the temperature. Below $T_N = 39$ K, the χ^{-1} values match a Curie−Weiss law $\chi(T) = C/(T - \theta)$ with $C = 8.73$ emu·K·mol^{-1} ($\mu_{eff} = \sqrt{8C} = 8.36$ μB/formula unit) and $\theta = -50.9$ K; the latter negative Weiss constant is in good agreement with the setting of a 3D AF ordering below $T_N = 39$ K. If one considers low spin (LS) Co^{III} ($S = 0$) for the trivalent positions (Co1, Co2, Co4), it yields $\mu_{eff} = 4.83$ μB/Co^{II} (Co3, Co5 being divalent) in good agreement with the common value for both tetrahedral Co^{II} ($eg^4\ t_{2g}{}^3$, $S = 3/2$) and high spin (HS) octahedral Co^{II} ($t_{2g}{}^5$, eg^2, $S = 3/2$). The significant deviation from the spin-only 3.87 μB theoretical value is likely due to an important unquenched orbital contribution, for example, $\mu_{eff\ oct}Co^{II} = 5.4$ μB and 5.32 μB

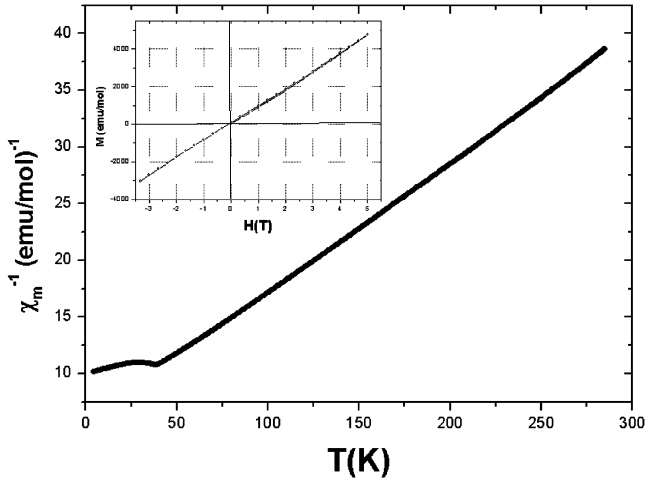

Figure 5. χ^{-1} versus *T*. The magnetization at 4K (inset) shows no residual F moment.

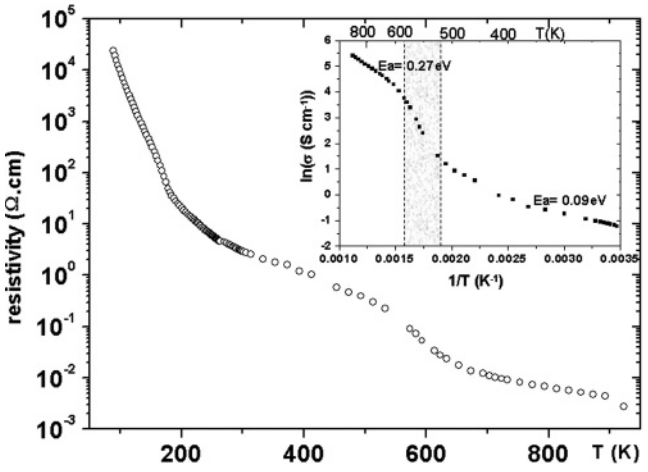

Figure 6. Electric resistivity evolution versus temperature: conductivity evolution $\ln(\sigma) = f(T)$ (inset) shows a broad transition between ∼200° and ∼400°.

in $CoMoO_4$[34] and $SeCoO_3$[35] and $\mu_{eff\ tet}Co^{II} = 5.4$ μB in the Co_3O_4 spinel.[36] Note that recent moment calculations in CoO have shown spin/orbital moment contributions of 2.64/1.38 μB at 0 K.[37] Finally, the magnetization plot at $T = 5$ K shows no contribution of residual magnetic moment, inset of Figure 5.

The electric resistivity versus temperature is plotted in Figure 6. It shows an increase of ρ on cooling from $\sim 3 \times 10^{-3}$ to $\sim 3 \times 10^4$ Ω·cm before 100 K, characteristic from a semiconducting behavior. Below 200 K, a discrepancy is observed which is currently under investigation. However, the material is clearly an insulator in this domain. At higher temperature, the plot of $\ln(\sigma)$ versus $1/T$ (inset Figure 6) shows two linear domains separated by a broad transition between 200 °C and 400 °C, that is starting of the reduction process by analogy to Figure 4a. The energies of activation

(34) Livage, C.; Hynaux, A.; Marrot, J.; Nogues, M.; Férey, G. *J. Mater. Chem.* **2002** *12*, 1423; *Phys. Rev. B* **2006**, *73*, 104442.
(35) Muñoz, A.; Alonso, J. A.; Martínez-Lope, M. J.; Morán, E.; Escamilla, R. *Phys. Rev. B* **2006**, *73*, 104442.
(36) Fukai, T.; Furukawa, Y. Y.; Wada, S.; Miyatani, K. *J. Phys. Soc. Jpn.* **1996**, *65*, 4067.
(37) Radwanski, R. J.; Ropka, Z. Orbital and spin moment in CoO. Available online: eprint http://arXiv.org/archive/cond-mat (0310622 V2, publication 11/2003).

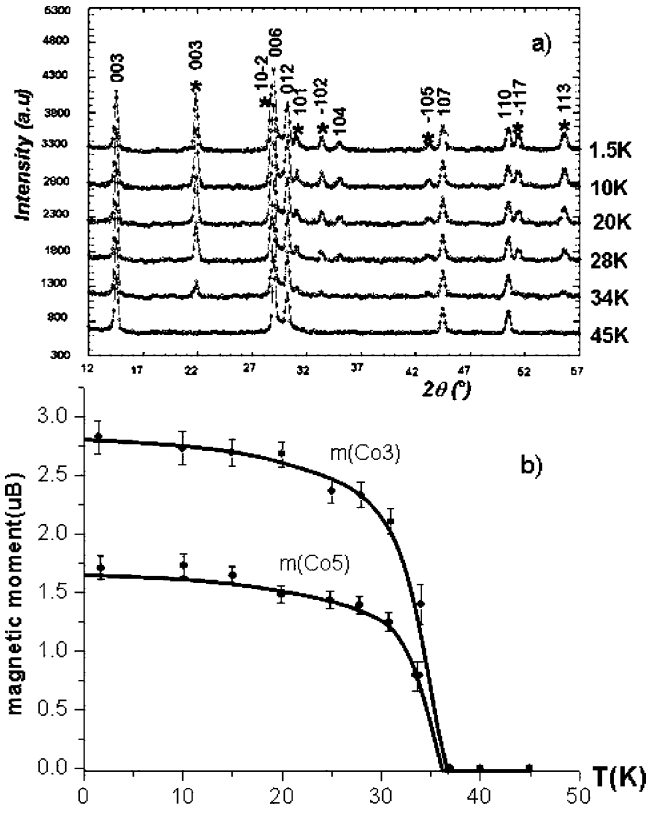

Figure 7. (a) ND pattern versus T with appearance of the magnetic satellites (*) and (b) refined magnetic moments of mCo3 (a) and mCo5 (b) below T_N.

for the two Arrhenius processes are 0.09 eV below 250 °C and 0.27 eV above 380 °C. These two domains should delimitate two distinct valence states within the crystal structure. Hence, considering the localized magnetic moments discussed below, a hopping process between Co^{II} and Co^{III} centers is expected. This particular feature suggests potential mixed conductivity processes in the medium-temperature range, currently under investigation.

Magnetic Structure. The ND pattern on cooling is shown in Figure 7a. Below T_N a series of magnetic satellite peaks grow. They can be indexed considering a unit doubled along c (propagation vector $\mathbf{k} = (0, 0, 3/2)$, accordingly to the R Bravais lattice). It can be related to the inversion and the conservation of the magnetic moments by the [2/3, 1/3, 1/3] and [1/3, 2/3, 2/3] translations, respectively; for example, see the magnetic analysis of $AgFe_3(SO_4)_2(OH)_6$ (space group $R\bar{3}m$, $k = (3/2)c^*$).[38] In a second stage, the analysis of the magnetic contributions shows a maximal peak for the 003 satellite and medium magnetic contributions for some general hkl satellites, while the $hk0$ do not show any magnetic satellites. According to the neutron/electron interaction process, these features imply magnetic moment lying in the a,b plane. Their possible arrangements have been investigated by using Bertaut's symmetry analysis method.[39,40] It has been performed using SARAh[41] by the calculation of the irreducible representations and basis magnetic vectors. Here, only the magnetic divalent Co3 and Co5 are concerned. Their positions in the asymmetric unit cell are Co3, (2/3, 1/3, ~0.57); Co3′, (1/3, 2/3, ~0.43); and Co5, (1/3, 2/3, 2/3). For each site, the representation of the propagation vector group can be decomposed upon six irreducible representations decomposed as follows:

Table 3. Results of the Magnetic Structure Refinement[a]

	reference atomic coordinates			magnetic vector		
atom	x	y	z	M (μB)	φ (deg)	θ (deg)
Co(5)	1/3	2/3	2/3	1.709(41)	0	90
Co(3)	2/3	1/3	0.56643(0)	2.829(35)	180	90
Co(3)′	1/3	2/3	0.43357(0)	2.829(35)	0	90

[a] $T = 1.5$ K, R_B(nucl) = 4.06%, R_B(magn) = 6.07%, $\chi^2 = 0.52$. The magnetic vectors are described in spherical coordinates.

$$\text{Co3: 6(c): } 0\Gamma1^{(1)} + 1\Gamma2^{(1)} + 1\Gamma3^{(1)} + 0\Gamma4^{(1)} + 1\Gamma5^{(2)} + 1\Gamma6^{(2)}$$

$$\text{Co5: 3(a): } 0\Gamma1^{(1)} + 0\Gamma2^{(1)} + 1\Gamma3^{(1)} + 0\Gamma4^{(1)} + 1\Gamma5^{(2)} + 0\Gamma6^{(2)}$$

where the superscript (1) and (2) exponents denote the order of the representations.

Because both sites magnetically order together, the same irreducible representation must be involved, that is, $\Gamma3^{(1)}$ or $\Gamma5^{(2)}$ as the only possible representations. The corresponding spin configurations are

$$\Gamma3^{(1)}: \ \psi_1{}^{r} = S^{z}_{Co3} - S^{z}_{Co3'}; S^{z}_{Co5}$$

$$\Gamma5^{(2)}: \ \psi_2{}^{c} + \psi_3{}^{c} = S^{x,y}_{Co3} - S^{x,y}_{Co3'}; S^{x,y}_{Co5}$$

where r and c show real and complex basis vectors associated with $\Gamma3$ and $\Gamma5$, respectively.

In fact, in our case the imaginary parts are neither detailed nor taken into account because they are only involved in particular $\mathbf{k}$ vector cases and yield (co)sine or elliptic magnetic structures. As follows from our prior deductions of magnetic moments lying in the a,b planes, only the $\Gamma5$ configuration is available because $\Gamma3$ form antiferromagnets with z-magnetic moments only. $\Gamma5$ yields parallel moments lying in the a,b plane. The refinement has been satisfactorily performed using Fullprof 2000 with respect to the $\Gamma5$ model. Then, Co3 and Co3′ have antiparallel moments of 2.83(3) μB while Co5 is antiparallel to Co3, 1.70(4) μB. The results are listed in the Table 3. All the tested models deviating from this final model showed significant increase of the reliability factors. Specifically, the moments for Co1, Co2, and Co4 spontaneously converge to zero from whichever starting magnetic vector. As a matter of fact, the rotation of the whole magnetic structure of any angle around c does not modify the refinement. Figure 7b shows the evolution of refined m_{Co3} and m_{Co5} versus the temperature. As a matter of general interest, this theoretical approach of the magnetic structure is all the more efficient because it excludes every magnetic out-of-plane canting-like magnetic contribution in agreement with the linear magnetization below T_N. Furthermore, it can help to distinguish between questionable

(38) Wills, A. S.; Harisson, A.; Ritter, C.; Smith, R. C. *Phys. Rev. B* **2000**, *61*, 6156.
(39) Bertaut, E. F. *Acta. Crystallogr., Sect. A* **1968**, *24*, 217.
(40) Rousse, G.; Rodriguez-Carvajal, J.; Wurm, C.; Masquelier, C. *Chem. Mater.* **2001**, *13*, 4527.
(41) Wills, A. S. *Physica B* **2000**, *276−278*, 680 (program SARAh available from ftp://ftp.ill.fr/pub/dif/sarah/).

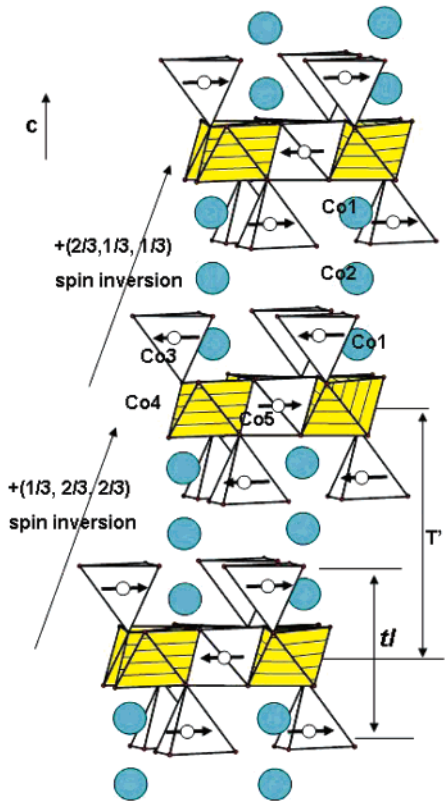

Figure 8. Magnetic structure for $Ba_2Co_9O_{14}$.

structural symmetries. For instance, in our case, the crystal structure refinement is possible in $R\bar{3}m$ (Co3 point symmetry: $3m$) and $R32$ (Co3 point symmetry: 3) with comparable R from room-temperature data. Hence, the possible loss of the center of symmetry through a slight displacive transition at lower temperature would not be detected by ND. However, in the acentric $R32$ space group, the representation of the propagation vector group is not compatible with the observed magnetic structure because it can only lead to a,b magnetic moments 120° rotated from each other, but no antiparallel vectors are authorized in the basal plane.

Analysis of the Magnetic Interactions. The magnetic structure for $Ba_2Co_9O_{14}$ is shown in Figure 8. It can be viewed as the AF stacking of ferrimagnetic triple layered (tl) blocks. The metal−metal magnetic interactions consist of Co−O−O−Co SSE only. This characteristic of the title compound, even if not unique (e.g., see the AF ordering below T_N = 34 K in the spinel Co_3O_4 by SSE-only interactions between Co^{II} diluted in a LS Co^{3+} network[36]), is sufficiently rare to be highlighted hereby. It is well-known that SSE interactions, which involve rather long intermetallic separations, can be stronger than shorter M−O−M superexchange paths. As a pertinent example, in the vanadyle vanadate $(Sr,Pb)_2(VO)(VO_4)_2$ with $S = 1/2$ chains it has been shown that the $V^{4+}-V^{4+}$ SSE through VO_4 groups is two orders of magnitude greater than V−O−V SSE.[42−44] Similarly, in the well-known $(VO)_2P_2O_7$ compound, the model based on alternating $S = 1/2$ AF chains correctly describes the system,[45−47] so-refuting the previously announced spin−ladder model.[48,49] In fact, the strong inter-ladder SSE exchanges excel super exchanges along the ladder legs. However, except from theoretical analyses such as extended Hückel tight binding calculations, there is no reliable consensus to estimate the sign and strength of SSE interactions. At the least, Whangbo et al. have established the important role of the O−O distances on SSE strengths as well as geometrical parameters playing on the overlap between the transmitting oxygen 2p orbitals of the O−O contacts.[50,51]

An exhaustive list of the geometrical parameters of the various $Co^{II}-O-O-Co^{II}$ AF and ferromagnetic (F) paths in $Ba_2Co_9O_{14}$ are reported in the Table 4. Because the interaction should rapidly decrease for O−O separation greater than the sums of the Van der Waals radii,[52] that is, d(O−O) > 2.8 Å, only the shorter Co5−O3−O2−Co3 is retained between these two metallic centers; see Table 4. Then the probable orbital overlap is shown in Figure 9a, where the oxygen 2p orbital lobes have been estimated from their σ-type overlapping with the t_{2g} of the closest cobalt ions. As an exception, the regular Co_4 tetrahedron around O2 suggests a sp^3 hybridization for this anion. The degree of imbrications is such that each Co5 interacts with three Co3 via two equivalent SSE paths. On the same figure is shown the F Co5−O3−O3−Co5 SSE path (six neighbors with two paths for each).

The AF Co3−O1−O1−Co3 SSE path is more questionable because it involves long O1−O1 distances of 2.936 Å, but one should remember the influence through the inter-tl block paths of the assisting dipolar interaction between the spontaneous moments of each ferrimagnetic tl block (Figure 8). The orbital overlapping for both AF inter-tl and F intra-tl is shown in Figure 9b. Finally it is worth mentioning that all the F SSE paths only involve overlapping angles of 120°. However, taking into account the rather long F Co−Co distances, 5.696 Å, they could be considered as purely virtual and the in-plane F ordering may be viewed as a geometrical effect of the 3D AF inter-tl Co3−Co3 and intra-tl Co5−Co3 ordering.

Considering both the abrupt setting of the magnetic ordering below T_N without prior deviation from the Curie−Weiss law and that each magnetic Co^{II} cation is surrounded by six AF Co^{II}, one could estimate an average exchange value between the Co neighbors. Within the mean field approximation, the Curie−Weiss temperature is given by $\theta = S(S+1)ZJ/3k_B$ where $S = 3/2$ for high spin Co^{II}, J is the

(42) Mentré, O.; Dhaussy, A. C.; Abraham, F.; Steinfink, H. *J. Solid State Chem.* **1998**, *140*, 417.
(43) Mentré, O.; Dhaussy, A. C.; Abraham, F.; Suard, E.; Steinfink, H. *Chem. Mater.* **1999**, *11*, 2408.
(44) Schmidt, B.; Yushankhai, Y.; Siurakshina, L.; Thalmeier, P. *Eur. Phys. J. B* **2003**, *32*, 43.
(45) Koo, H. J.; Whangbo, M. H.; VerNooy, C. C; Torardi, W. J.; Marshall, W. J. *Inorg. Chem.* **2002**, *41*, 4664.
(46) Garret, W. A.; Nagler, S. E.; Tennant, D. A.; Barnes, T. *Phys. Rev. Lett.* **1997**, *79*, 745.
(47) Kikuchi, J.; Motoya, K.; Ueda, Y. *Phys. Rev. B* **1999**, 6731.
(48) Eccleston, R. S.; Barnes, T.; Brody, J.; Johnson, J. W. *Phys. Rev. Lett.* **1994**, *73*, 2626.
(49) Barnes, T.; Riera, J. *Phys. Rev. B* **1994**, *50*, 6817.
(50) Whangbo, M.-H.; Koo, H.-J.; Dai, D. *J. Solid State Chem.* **2003**, *176*, 417.
(51) Koo, H. J.; Whangbo, M. H.; Vernoy, P. D.; Torardi, C. C.; Marshall, W. J. *Inorg. Chem.* **2002**, *47*, 4664.
(52) Whangbo, M. H.; Dai, D.; Koo, H. J. *Solid State Sci.* **2005**, *7*, 827.

Table 4. Geometrical Parameters Associated with the SSE Path Co−O···O−Co[a]

between the Co_3 atoms (antiferro)

SSE path	CoHCo (Å)	O···O (Å)	∠Co−O···O (deg)	∠O···O−Co (deg)
(X2 X3) $Co_3-O_1-O_1-Co_3$ I	5.081	2.936	122.2	122.2

between the Co3 atoms (ferro)

SSE path	CoHCo (Å)	O···O (Å)	∠Co−O···O (deg)	∠O···O−Co (deg)
(X1 X6) $Co_3-O_1-O_1-Co_3$ II	5.696	2.551	144.4	144.4

between the Co_5 and Co_3 atoms (antiferro)

SSE path	Co···Co (Å)	O···O (Å)	∠Co_5−O···O (deg)	∠O···O−Co_3 (deg)
(X2 X6) $Co_5-O_3-O_1-Co_3$ I	4.375	2.879	132.5	86.5
(X1 X6) $Co_5-O_3-O_2-Co_3$ I	**4.375**	**2.546**	**94.9**	**143.5**
(X1 X6) $Co_5-O_3-O_2-Co_3$ II	4.375	2.854	86.4	87.4

between the Co_5 atoms (ferro)

SSE path	Co···Co (Å)	O···O (Å)	∠Co_5−O···O (deg.)	∠O···O−Co_5 (deg.)
(X2 X6) $Co_5-O_3-O_3-Co_5$	5.696	2.619	137.5	137.5

[a] In X*x* and X*y*, *x* denotes the number of equivalent O−O paths for each Co*a*, Co*b* pair, while *y* denotes the number of equivalent Co*b* atoms around Co*a*.

spin exchange value, and *Z* is the number of nearest neighbor magnetic ions around the central site, $Z = 6$. With $\theta = -50.9$ we obtain $J/k_B = -4.8$ K.

The observed values for the moment of Co^{II} are strongly dependent on several parameters including the orbital contribution and the effects of covalence. In $Ba_2Co_9O_{14}$, the difference of magnitude of the moments of the tetrahedral Co3 (2.83(3) μB) and the octahedral Co5 (1.71(4) μB) should be mainly related to the degree of covalence with the surrounding oxygen ions involved in the SSEs; for example, a significant influence of each oxygen corner should reduce the localized moment especially when not directly connected to another magnetic ion. Then, Co3 shows a moment comparable with the tetrahedral Co^{II} in Co_3O_4 also involved in SSE only, $m = 3.26$ μB from ND.[53] Co5 has a much smaller moment and is surrounded by six oxygen ions strongly involved in bonds with diamagnetic Co^{III} actions. This situation inevitably leads to a $Co^{II} \rightarrow O$ covalent magnetic transfer. For instance, in β-$CoMoO_4$, isolated octahedral trimers order antiferromagnetically by SSE below 6 K, $mCo^{II} = 1.35-1.5$ μB determined by ND.[54] For the latter, the high pressure β-form modification leads to infinite edge-sharing chains of $Co^{II}O_6$ octahedra that order antiferromagnetically by SSE under $T_N = 68$ K, with $mCo^{II} = 3.7$ μB from ND.[55] This increase of m_{Co} is a sensitive indication of the relative SE/SSE ratio in the 3D magnetic arrangement. As a matter of fact, in CoO in which each cobalt shares edges with 18 neighbors, a higher moment = 3.98 has been refined from ND at 40 K.[56]

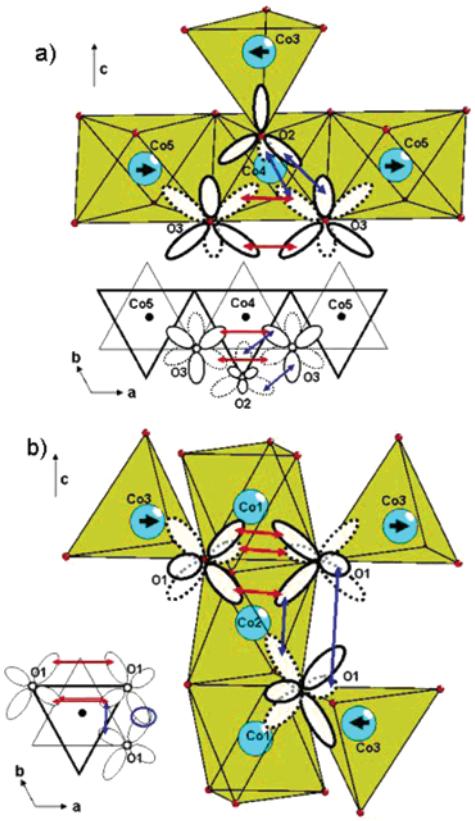

Figure 9. Probable overlap of the oxygen atom orbitals through the SSE paths: (a) Co3−O2−O3−Co5 and Co5−O3−O3−Co5 and (b) Co3−O1−O1−Co3.

Concluding Remarks

The discovery of the new $Ba_2Co_9O_{14}$ is particularly interesting at several exciting levels. First, from the structural point of view, it displays an original structural type containing the new T′ building blocks by analogy with the T-blocks of the Ba-hexaferrites. The potential construction of original materials formed from the intergrowth of T′ and additional 3D entities opens a wide field of investigation within the quest of new oxides. Our exhaustive characterization has shown the presence of magnetic Co^{II} cations interacting through SSEs only surrounded by low-spin Co^{III}. In addition, the analysis of the exchanges in competition and of the magnetic structure reveals the influence of the Co−O covalence on the localized magnetic moments. At high temperature the behavior is all the more interesting, because the reversible partial reduction upon heating suggests oxygen

(53) Roth, W. L. *J. Chem. Solids* **1964**, *25*, 1.
(54) Wiesmann, M.; Ehrenberg, H.;Wltschek, G.; Zinn, P.; Weitzel, H.; Fuess, H. *J. Magn. Magn. Mater.* **1995**, *150*, L1.
(55) Ehrenberg, H.;Wiesmann, M.; Garcia-Jaca, J.; Weitzel, H.; Fuess, H. *J. Magn. Magn. Mater*. **1998**, *182*, 152.
(56) Jauch, W.; Rehuis, M.; Bleif, H.; Kubanek, F. *Phys. Rev. B* **2001**, *64*, 052102.

transport properties and possible mixed ionic/electronic mobility in the medium-temperature range. This electrochemical aspect is currently under investigation in SOFC electrode working conditions. Finally, the original decomposition and reformation of the title compound in $BaCoO_{3-\delta}$ and CoO upon cooling/heating cycles indicates the possible use of alternative synthesis methods from the mixture of original precursors for mixed valent cobalt oxides.

Acknowledgment. M.C. thanks the Division of Structural Chemistry (Stockholm University) for microscopy facilities. The Laboratoire Leon Brillouin and Dr. Emmanuelle Suard of the Institut Laue Langevin are thanked for access to the neutron diffraction facility. The "Fonds Européen de Développement Régional (FEDER)", "CNRS", "Région Nord Pas-de-Calais", and "Ministère de l'Education Nationale de l'Enseignement Supérieur et de la Recherche" are acknowledged for funding of the X-ray diffractometers.

Supporting Information Available: The atomic coordinates for $Ba_2Co_9O_{14}$, the redox titration process, the results of the room-temperature ND refinement, and additional graphs and tables related to this work (PDF) and the CIF file. This material is available free of charge via the Internet at http://pubs.acs.org.

CM062897Q